Scientific Research Publishing

American Journal of Analytical Chemistry, 2017, 8, 60-71
http://www.scirp.org/journal/ajac
ISSN Online: 2156-8278
ISSN Print: 2156-8251

Influence of Mn Doping on the Sensing Properties of SnO_2 Nanobelt to Ethanol

Jieqing Huang[1,2], Yingkai Liu[1,2,3*], Yuemei Wu[1,2], Xinmin Li[1,2]

[1]Key Laboratory of Yunnan Higher Education Institutes for Optoelectric Information & Technology, Kunming, China
[2]Institute of Physics and Electronic Information, Yunnan Normal University, Kunming, China
[3]Key Laboratory of Yunnan Normal University for Photoelectric Materials & Device, Kunming, China
Email: huangjieqing608@163.com, *ykliu@ynnu.edu.cn, wuyuemei893@163.com, lixinmin809@163.com

How to cite this paper: Huang, J.Q., Liu, Y.K., Wu, Y.M. and Li, X.M. (2017) Influence of Mn Doping on the Sensing Properties of SnO_2 Nanobelt to Ethanol. *American Journal of Analytical Chemistry*, **8**, 60-71.
http://dx.doi.org/10.4236/ajac.2017.81005

Received: December 7, 2016
Accepted: January 9, 2017
Published: January 12, 2017

Abstract

Mn doped SnO_2 nanobelts (Mn:SnO_2 NBs) and pure SnO_2 nanobelts (SnO_2 NBs) were synthesized by thermal evaporation technique at 1355˚C with Ar carrier gas (25 sccm, 150 Torr). The SEM, EDS, XRD, TEM, HRTEM, SAED, XPS, UV-Vis techniques were used to characterize the attained samples. The band gap of Mn doped SnO_2 NBs by UV-Vis was measured to be 3.43 eV at room temperature, lower than that of the pure counterpart with ~3.66 eV. Mn:SnO_2 NB and pure SnO_2 NB sensors were developed. It is found that Mn:SnO_2 NB device exhibits a higher sensitivity with 62.12% to 100 ppm of ethanol at 210˚C, which is the highest sensitivity among the three tested VOC gases (ethanol, ethanediol, and acetone). The theoretical detection limit for ethanol of the sensor is 1.1 ppm. The higher response is related to the selective catalysis of the doped Mn ions.

Keywords

SnO_2 Nanobelts, Mn^{3+} Doping, Gas Sensor, Single Nanobelt Device

1. Introduction

Metal-oxide semiconductor gas sensors have been used to detect gases for their efficiency and spread applicability [1] [2]. In particular, one-dimensional semiconductor nanostructures, such as nanobelt, nanowire and nanotube, due to their unique physical and chemical properties caused by their nanometer size effect, have aroused great interest due to their unique characteristics [3] [4] [5] [6] [7]. Therefore, metal-oxide semiconductor nanostructured materials, such as SnO_2, In_2O_3, WO_3 and ZnO, have been widely manufactured as sensors for de-

tecting air composition and organic or poisonous gases due to low cost, easy accessibility, high performance, and reliable stability [8] [9] [10] [11]. Among them, SnO_2 with a band gap (3.6 eV), has high sensitivity and fast response [12]. Hence, SnO_2 nanomaterials have been investigated to detect many gases, such as ethanol, H_2S, and so on [13] [14] [15]. It is well known that the dopant of rare metals may improve the sensitive performance of nanomaterials [16]. For instance, Li *et al.* have reported that the sensitivity of Er-doped SnO_2 nanobelt device is 9 to the formaldehyde gas [17]. Ma *et al.* have found that the response of Sb-doped SnO_2 nanoribbon device reaches 56 (10) to 100 ppm (ppb) of H_2S at 150˚C and 19 (1.6) to 100 ppm (ppb) of H_2S at 25˚C [18].

Doping enhances the properties of semiconductors by providing a powerful strategy to control their optical, electronic, transport, and spintronic properties [19]. The optoelectronic properties such as photoluminescence and optical band gap of SnO_2 can also be improved by metals doping. Many studies were reported on the SnO_2 doped by Sb, In, and Mn etc. [20] [21] [22]. Much emphasis is put on manganese (Mn) due to its large equilibrium solubility and nearly the same ionic radii as with Sn^{4+} ion for substitution.

In this paper, we systemically investigated the sensing and optical properties of a single Mn:SnO_2 NB sensor to volatile organic (VOC) liquids and reported interesting results.

2. Experimental Section

2.1. Synthesis and Characterization of SnO_2 NBs and Mn:SnO_2 NBs

Single SnO_2 and Mn:SnO_2 NBs were obtained by thermal evaporation method. For the synthesis of Mn:SnO_2 NBs, the mixture of pure SnO_2 powders (>99.99 wt.%) and $MnC_2O_4{\cdot}2H_2O$ powders premixed in the weight ratio of 20:1 was put into a ceramic boat. The ceramic boat was placed into the central position of the horizontal alundum tube, which was put into a high temperature furnace. A silicon substrate coated with about 10 nm Au film was placed into the tube, the distance of silicon substrate and ceramic boat was about 15 cm. After cleaning the tube several times with nitrogen gas, the tube was evacuated by a mechanical pump to a pressure of 1 to 5 Pa. The precursors of SnO_2 and $MnC_2O_4{\cdot}2H_2O$ powders were maintained at 1355˚C for 2 h and deposited on the Si substrate with Ar carrier gas (25 sccm, the pressure inside the tube is 150 Torr). After the furnace was cooled to room temperature naturally, white wool-like products were obtained. In order to compare the sensing properties of Mn:SnO_2 NBs and pure SnO_2 NBs, we also prepared pure SnO_2 NBs by similar method.

The nanobelts were characterized by scanning electron microscopy (SEM) and energy-dispersive X-ray spectroscopy (EDS), X-ray diffraction (XRD), transmission electron microscopy (TEM) and high-resolution electron microscopy (HRTEM), selected area electron diffraction (SAED), X-ray photoelectron spectrometer (XPS), and ultraviolet and visible spectrophotometer (UV-Vis).

2.2. The Manufacture and Characterization of a Single Nanobelt Gas Sensor

SnO_2 NBs and Mn:SnO_2 NBs were picked out and then dispersed into ethanol by the tweezers. A few of the resulting suspensions were dropped onto a silicon substrate with thickness of a 500 nm SiO_2 layer. The suspensions dried naturally and led to the nanobelts stick to the substrate closely. The mask plate was placed on the top of this substrate to prepare the electrodes. Patterned Ti (10 nm) and Au (100 nm) electrodes were successively deposited on the nanobelts in high vacuum by dual-ion beam sputtering (LDJ-2a-F100-100 series) with Ar carrier gas (10 mA/cm^2, 2.2×10^{-2} Pa).

The measurement of the gas sensor was processed with the equipment designed by our laboratory [23]. The process was conducted in a hermetic stainless steel box (20 L). Then, the device was put on a heating station, on which its temperature can be accurately controlled. The sensing properties of the device were measured by Keithley 4200 semiconductor test system. The applied bias voltage was 1 V and the testing interval was 200 seconds. The target liquid can be injected into a heater to evaporate the VOC liquid violently and the fan was used to produce a homogeneous atmosphere in the chamber. The optical microscopic image of a single nanobelt device is displayed in Figure 1.

3. Results and Discussion

3.1. Structural Characterization

3.1.1. SEM and HRTEM

The morphology of the as-synthesized materials is displayed in Figure 2. Mn:SnO_2 NBs and SnO_2 NBs have similar morphology. Figure 2(a), Figure 2(b) are SEM micrographs of Mn:SnO_2 NBs by low and high magnifications. The product consists of a large quantity of ribbon-like structures with different thickness and width, as shown in Figure 2(a). Most of the nanobelts have uniform thickness and width. Figure 2(b) depicts that their thickness is less than

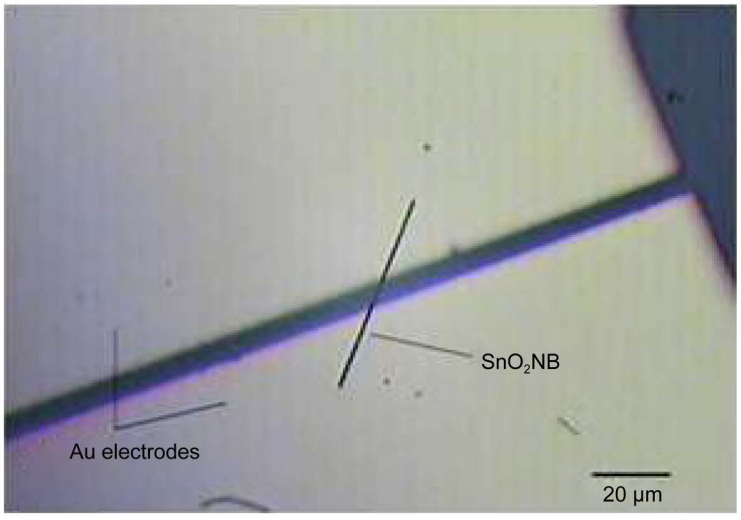

Figure 1. The microscope photograph of a prepared SnO_2 NB device.

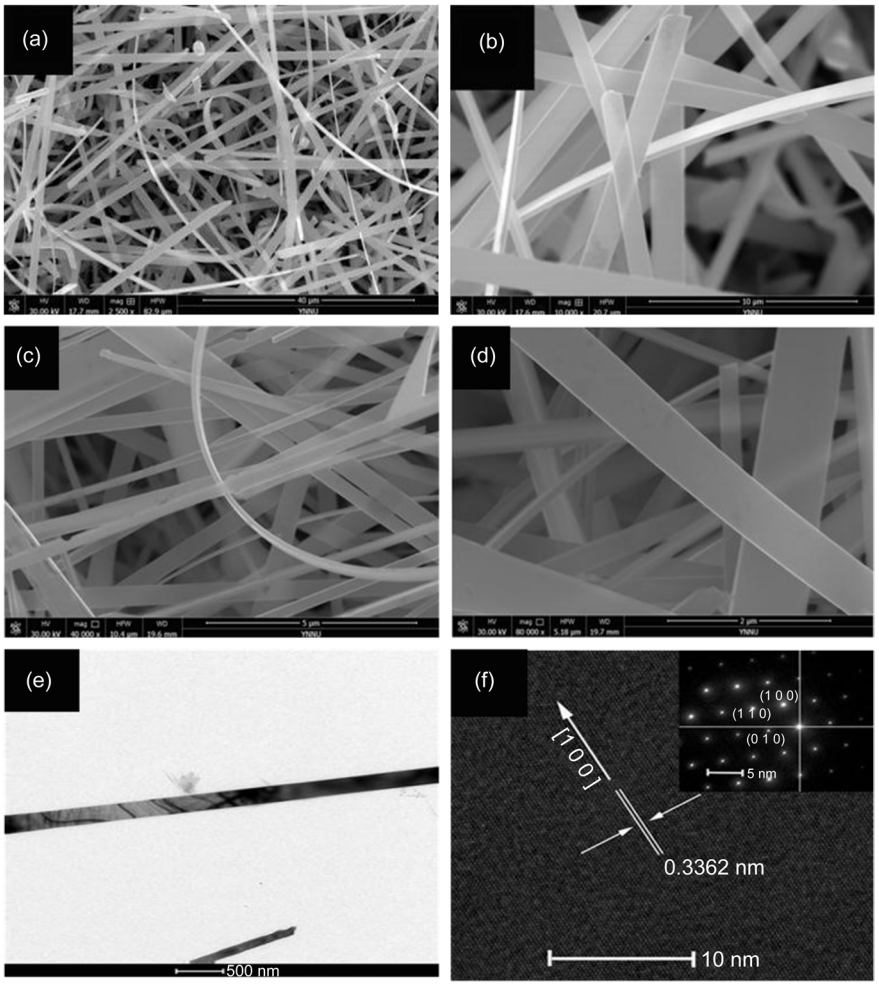

Figure 2. (a) Low and (b) high magnification SEM micrograph of Mn:SnO_2 NBs. (c) Low and (d) high magnification SEM micrograph of SnO_2 NBs. (e) TEM image of Mn:SnO_2 NB. (f) HRTEM image of Mn:SnO_2 NB, its inset is SAED pattern.

100 nm, the width is from 250 nm to 1 μm, and the length is about 50 μm. It is also seen that the Mn:SnO_2 NBs have a good shape with smooth surface, which are suitable for preparing gas sensors. Figure 2(c) is SEM image of SnO_2 NBs by low magnification, it can be obviously seen that the SnO_2 NBs are band-like structure, the length of them is about 30 - 100 μm. Figure 2(d) is a high magnification SEM micrograph of SnO_2 NBs, the SnO_2 NBs have smooth surface, the width is less than 1 μm, and thickness is about 50 - 100 nm.

For further characterizing their microstructure, we carried out TEM, HRTEM and SAED examination and are presented in Figure 2(e) and Figure 2(f). TEM image illustrates that the width of a selected NB is about 300 nm. Figure 2(d) presents HRTEM image of a single Mn:SnO_2 NB and its corresponding SAED pattern. It is seen that the interplanar spacing is 0.3362 nm, matching with the (1 0 0) plane for tetragonal structure SnO_2, no defects have been detected. The regular arrangement of the diffraction spots is shown in the upper-right inset of Figure 2(d), revealing that the growth direction of Mn:SnO_2 NBs is along [1 0 0].

3.1.2. XRD and EDS

XRD pattern of Mn:SnO_2 NBs is presented in **Figure 3(a)**. The diffraction peaks can be indexed as the tetragonal structure SnO_2 with lattice parameters a = b = 0.4738 nm, c = 0.3189 nm (JCPDS file No. 71-0467).

In order to decide whether Mn ions were doped into SnO_2 NBs or not, energy-dispersive X-ray diffraction spectroscopy (EDS) pattern of a single Mn:SnO_2 NB is conducted, as shown in **Figure 3(b)**. It is seen that the doped Mn ions content of SnO_2 NBs is only 1.64 at.%. The Sn and O atomic percentage is 1:1.8, which is smaller than tin dioxide stoichiometric ratio (1:2), indicating that there are oxygen vacancies in the sample.

3.1.3. XPS Analysis

The XPS observation of as-prepared Mn:SnO_2 sample is shown in **Figure 4(a)**. From the global XPS profiles, the lines related to Sn, O, Mn, and C elements are observed. Carbon is ubiquitously presented on all surfaces for XPS spectra. It is well known that the peak at 285.0 eV of carbon C 1 s is used as a reference for charge correction. The Sn(3d) band presents double peaks located at binding energies of 487.0 of Sn($3d_{5/2}$) and 495.4 eV of Sn($3d_{3/2}$), as shown in **Figure 4(b)**. The separation distance between the two peaks is 8.4 eV, which confirms the formation of Sn^{4+} oxidation state in SnO_2 nanobelts [24]. The Mn (2p) state can be separated into two peaks. One is centered at 640.0 eV, the other at 644.9 eV, as displayed in **Figure 4(c)**.

The deconvolution of the O (1s) peak shows two Gaussian peaks centered at 530.9 and 531.7eV, respectively (as illustrated in **Figure 4(d)**). The peak located at the lower binding energy corresponds to the O (1 s) core peak of O^{2-} bound to Sn^{4+} and the other one at higher binding energy originates from O defects [25].

$$\frac{n_{Sn}}{n_O} = \frac{I_{Sn}}{I_O} \times \frac{S_O}{S_{Sn}}$$

S_{Sn} and S_O are sensitive factors (S_{Sn} = 4.095, S_0 = 0.711); I_{Sn} and I_O are the peak areas; n_{Sn} and n_O are atomic concentrations on behalf of *Sn* and *O* elements, respectively. The ratio of n_{Sn} and n_O is 0.56 by fitting. However, the ratio of n_{Sn} and n_O in pure SnO_2 is 0.5. It is further corroborated that the Mn:SnO_2 NBs have oxygen vacancies.

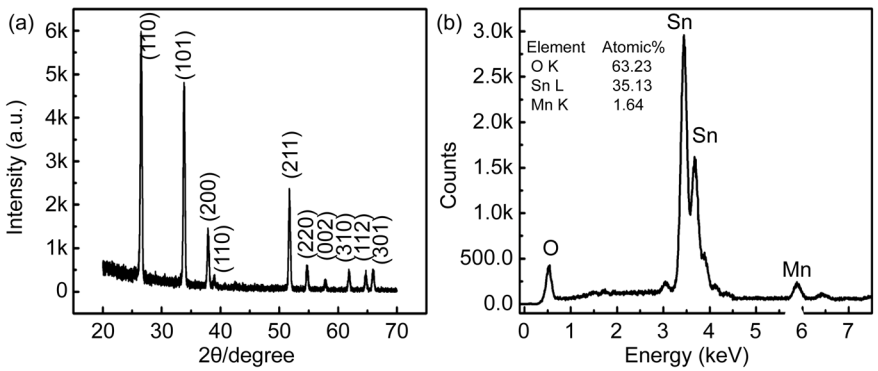

Figure 3. (a) XRD of Mn:SnO_2 NBs. (b) EDS of Mn:SnO_2 NB.

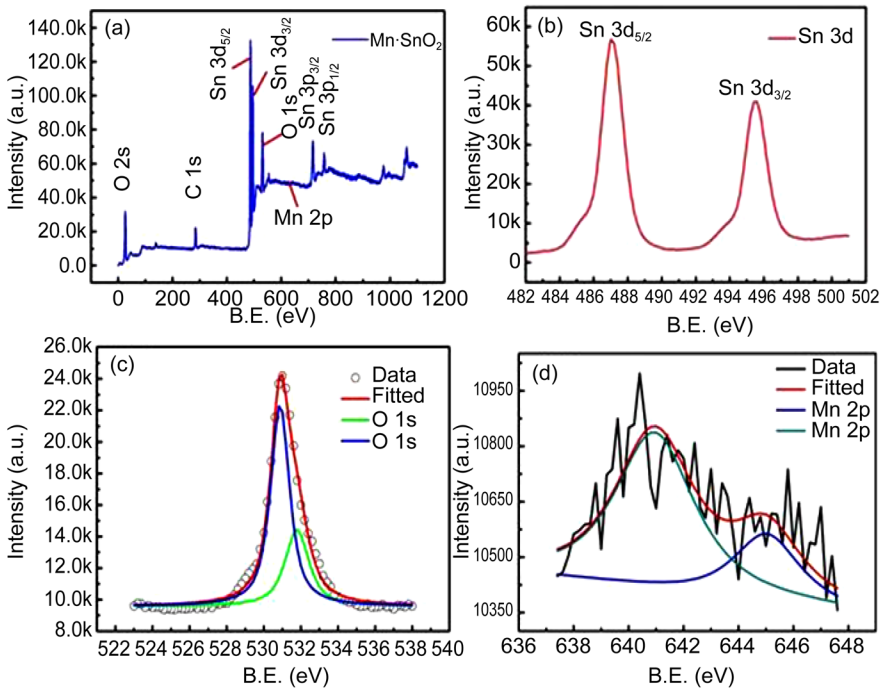

Figure 4. XPS spectra of the Mn:SnO_2. (a) global survey spectra and high-solution (b) Sn 3d, (c) O 1 s and (d) Mn 2p spectrum.

3.2. UV-Vis Spectra

The optical absorption coefficient α of a semiconductor close to the band edge can be expressed by the following Wood-Tauc Equation [26]:

$$\alpha = k\left(h\nu - E_g\right)^n / h\nu$$

where α is the absorption coefficient, k is a constant about material properties, $h\nu$ is the energy of a photon, E_g is band gap, and n is a parameter that depends on the nature of the transition. In this case, n is equal to 1/2 for a direct bandgap material. The band gap can be estimated from a plot of $(\alpha h\nu)^2$ versus photon energy.

Figure 5 shows the absorption spectra of Mn:SnO_2 NBs and SnO_2 NBs. The band gaps (Eg) of Mn:SnO_2 NBs and SnO_2 NBs are 3.43 and 3.66 eV, respectively. The shift may be due to the quantum size effect. The plots of $(\alpha h\nu)^2$ as a function of the energy ($h\nu$) of the incident radiation for Mn:SnO_2 NBs and SnO_2 NBs are presented in the inset of **Figure 5**. All plots show non-linear nature. Compared with that of SnO_2 NBs, the redshift is observed in the absorption edge of Mn:SnO_2 NBs. The change on the bandgap suggests that the size of the nanobelt has an influence on the optical properties of the materials, which can be tuned by doping.

3.3. Sensing Properties

The sensor's response is defined as the relative change of resistance in the surrounding gas atmosphere divided by the resistance in synthetic air [27], which is defined as

$$S\% = \frac{Ra - Rg}{Ra} \times 100\% = \left(1 - \frac{Rg}{Ra}\right) \times 100\%$$

In the formula of $S(\%)$, R_a is the sensor resistance in the air and R_g is the resistance in the tested gas.

The curves exhibit a linear shape, so both doped and pure NBs possess a good Ohmic contact, as shown in Figure 6. The slope of pure SnO_2 NB is less than that of Mn:SnO_2 NB. The resistances of Mn:SnO_2 NB and its pure counterpart are about 1.65×10^8 Ω and 1.61×10^9 Ω respectively at 210˚C, indicating that the resistance of SnO_2 is greatly reduced after doping.

Upon exposed to 100 ppm of ethanol, ethanediol, and acetone gases, the responses of the sensors based on Mn:SnO_2 NB and its undoped counterpart have been tested as a function of the temperatures from 50˚C to 300˚C, as shown in Figure 7(a), Figure 7(b). The best operating temperature of Mn:SnO_2 NB to the three gases is 210˚C and the responses to ethanol, ethanediol, and acetone are

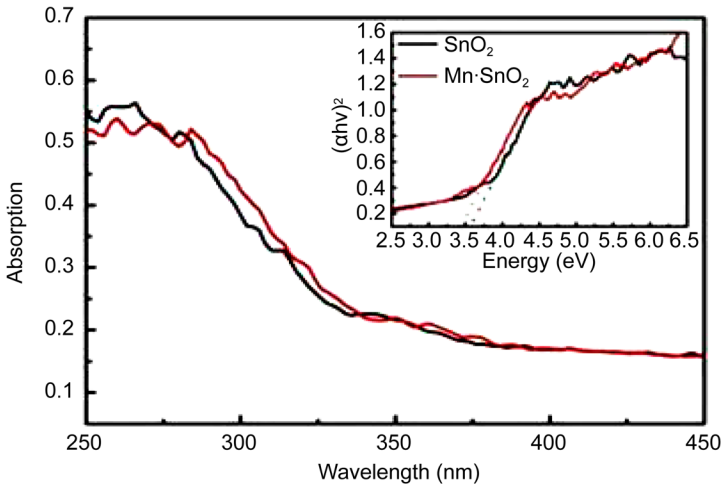

Figure 5. The UV absorption spectra of Mn:SnO_2 NBs and SnO_2 NBs.

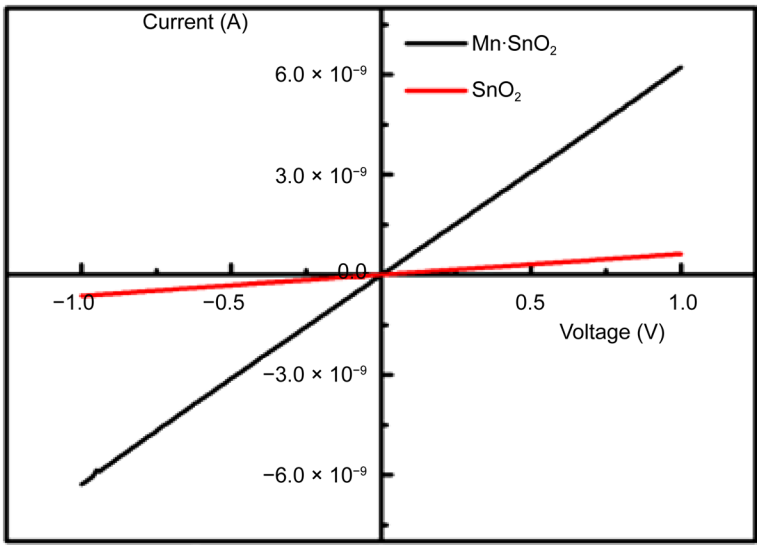

Figure 6. I-V curves of pure SnO_2 NB and Mn:SnO_2 NB devices.

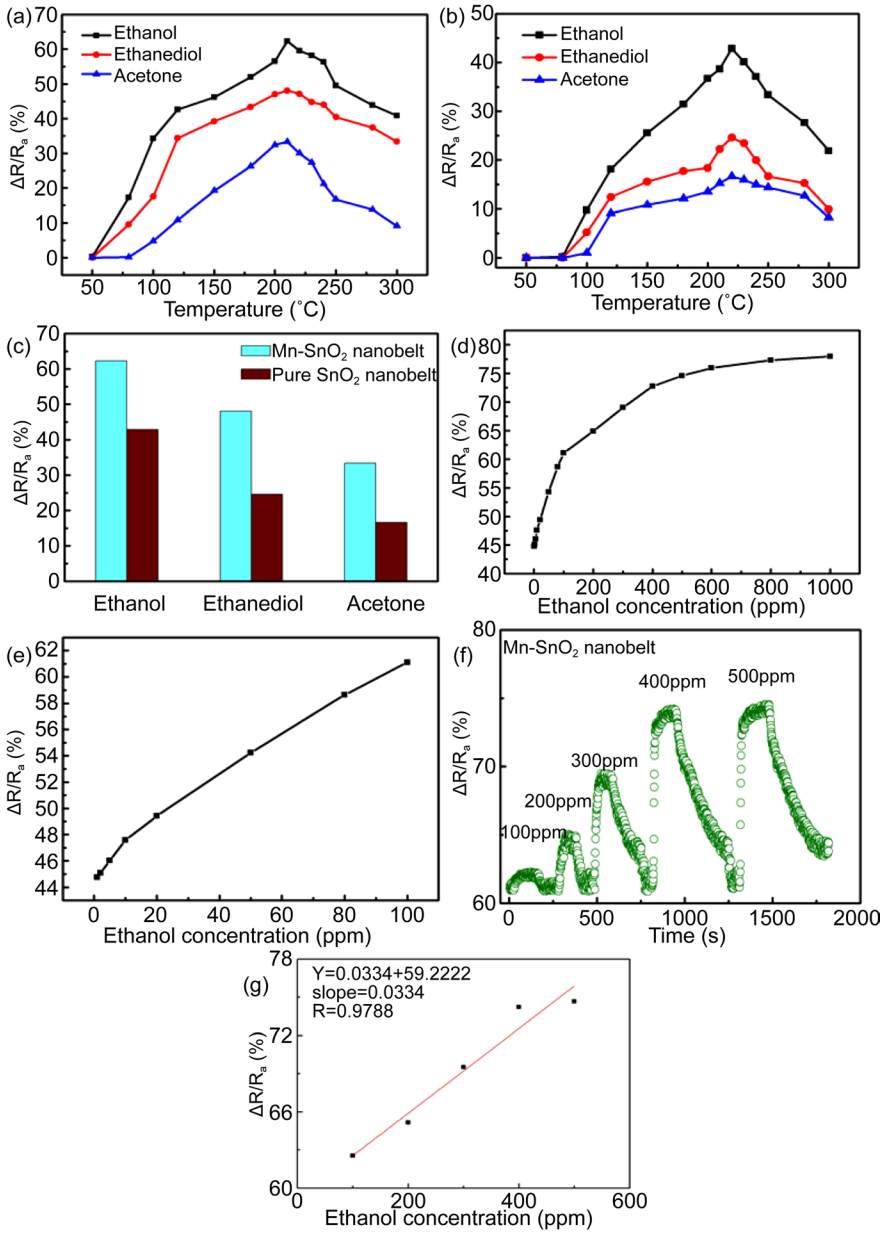

Figure 7. (a) and (b) The gas sensitivity of Mn:SnO_2 NB and pure SnO_2 NB to 100 ppm of various gases at different temperature; (c) Histogram sensitive responses of Mn:SnO_2 NB and pure SnO_2 NB at 210˚C; (d) The sensitivity of Mn:SnO_2 NB to ethanol from 5 to 1000 ppm at 210˚C; (e) The curve of response versus ethanol concentration in the range of 5 - 100 ppm; (f) Responses to 100 - 500 ppm of ethanol at 210˚C; (g) The fitting curve of response versus ethanol concentration in the range of 100 - 500 ppm.

62.12%, 47.92% and 33.33% respectively. However, the best working temperature of the SnO_2 NB to the three gases are 220˚C and its responses are only 42.86%, 24.24% and 16.67%. Obviously, the sensitivity of Mn:SnO_2 NB is much better than that of the latter, especially to ethanol. The best working temperature of Mn:SnO_2 NB is lower and the sensitivity to ethanol reaches 62.12%, far higher to the others. As evidenced from Figure 7(c), the sensitive responses of Mn:SnO_2 NB for ethanol, ethanediol and acetone are 1.51, 1.45, and 1.25 times as

large as those of pure SnO_2 NB. The results manifest that doping of Mn reduces the optimum working temperature, enhances the sensitivity effectively, and greatly improves the selectivity of SnO_2 NB.

The response of the Mn:SnO_2 NB has also been tested and are illustrated in **Figure 7(d)**, **Figure 7(e)** under ethanol from 10 to 1000 ppm at 210˚C. It is noted that the response increased drastically in the range of 10 - 100 ppm, then moderately in 100 - 600 ppm, and slowly in 600 - 1000 ppm. The response tends to become saturated when ethanol concentration goes up, which can be attributed to the surface coverage of the adsorbed molecules [24]. The response of Mn:SnO_2 sensors are provided upon repeatedly ethanol, ethanediol, and acetone gases exposure/removal cycles, as displayed in **Figure 7(f)**. Five cycles are successively recorded, corresponding to 100, 200, 300, 400, and 500 ppm of ethanol gase. For all testing cycles, the resistance returns completely to its original value once the gases are pumped out. It can be seen that Mn:SnO_2 NB has a high sensitivity to ethanol. The corresponding response/recovery time is about 18 s/20 s.

Figure 7(g) shows the fitting curve of response versus ethanol concentration in the range of 100 - 500 ppm. The response is approximately linearly, and the slope of it is 0.0334 ppm^{-1} with a fitting quality of $R = 0.9788$. The sensor noise is calculated by the variation of the relative response at the baseline with help of root-mean-square deviation (RMSD) [22] [23] [28]. Then, 200 data points (N) of **Figure 7(f)** are collected, and the standard deviation (S) is obtained as 0.17369. According to $RMS_{noise} = \sqrt{S^2/N}$, RMS_{noise} is 0.01228 for the ethanol sensor. Based on the signal-to-noise ratio using $DL(ppm) = 3 \times RMS_{noise}/Slope$, the theoretical detection limit for ethanol of the sensor is 1.1 ppm.

3.4. Gas Sensing Mechanism

As a solid material, the gas-sensing mechanism of SnO_2 sensor belongs to surface phenomenon [29]. It is well known that the gas sensing involves three key reaction processes: adsorption, oxidation, and desorption [30]. The oxygens are adsorbed in several species such as O_2^-, O^- and O^{2-} through Equations (1)-(4) [31].

$$O_2\ (\text{Gas}) \Leftrightarrow O_2\ (\text{adsorption}) \tag{1}$$

$$O_2\ (\text{adsorption}) + e^- \Leftrightarrow O_2^-\ (\text{adsorption}) \tag{2}$$

$$O_2^-\ (\text{adsorption}) + e^- \Leftrightarrow 2O^-\ (\text{adsorption}) \tag{3}$$

$$O_2^-\ (\text{adsorption}) + e^- \Leftrightarrow O_2^-\ (\text{adsorption}) \tag{4}$$

when ethanol liquid is injected into the equipment and then evaporates, its vapor contacts the sensor and reacts with the surface chemisorbed oxygen. The process is as follows:

$$C_2H_5OH + 3O_2^-\ (\text{ads}) = 2CO_2 + 3H_2O + 3e^- \tag{5}$$

$$C_2H_5OH + 6O^-\ (\text{ads}) = 2CO_2 + 3H_2O + 6e^- \tag{6}$$

$$C_2H_5OH + 6O^{2-}\ (\text{ads}) = 2CO_2 + 3H_2O + 12e^- \tag{7}$$

Obviously, many electrons are released and hence the resistance decreases during the reaction. In our work, the sensitivity to ethanol is availably improved by Mn ions. The reasonable sensitive improvement mechanism is proposed as follows. As shown as the results, Mn ions can promote the crystallinity of SnO_2 NBs. Besides, Mn doping can produce more oxygen vacancies and reduces the barrier height of the material [32].

$$Mn^{3+} + H_2O \rightarrow MnO^{+} + H^{+} \quad (8)$$

$$O_O^{\times} \leftrightarrow V_O^{\bullet\bullet} + 2e' + 1/2O_2 \quad (9)$$

$$2MnO^{+} + O_O^{\times} \rightarrow Mn_2O_3 + V_O^{\bullet\bullet} + 2e' \quad (10)$$

As expressed by Equations (8)-(10), Mn ions may enhance the surface dehydrogenation resulting in the oxidation of ethanol needs lower energy, so that the liberation of electrons will be promoted [33] [34]. Hence, the electric conductivity of SnO_2 NB increases.

4. Conclusion

Mn:SnO_2 NBs and pure SnO_2 NBs were synthesized by thermal evaporation. The band gap of Mn doped SnO_2 nanobelts by UV-Vis was measured and is 3.43 eV respectively at room temperature, lower than that of the pure SnO_2 NBs (~3.66 eV). SnO_2 NB and Mn:SnO_2 NB sensors were developed. It is found that the Mn:SnO_2 NB device exhibits a higher sensitivity of 62.12% to 100 ppm of ethanol at 210˚C, which is the highest sensitivity among the three tested VOC gases. The higher response is related to the selective catalysis of doped Mn ions.

Acknowledgments

This work was supported by the National Natural Science Foundation (Grant No. 11164034), the Key Applied Basic Research Program of Science and Technology Commission Foundation of Yunnan Province (Grant No. 2013FA035), and the Innovative talents of Science and Technology Plan Projects of Yunnan Province (Grant No. 2012HA007).

References

[1] Ahn, J.H., Yun, J., Choi, Y.K. and Park, I. (2013) Palladium Nanoparticle Decorated Silicon Nanowire Field-Effect Transistor with Side-Gates For Hydrogen Gas Detection. *Applied Physics Letters*, **104**, Article ID: 013508.

[2] Liu, X., Zhang, J., Yang, T., Guo, X., Wu, S. and Wang, S. (2011) Synthesis of Pt Nanoparticles Functionalized WO_3 Nanorods and Their Gas Sensing Properties. *Sensors and Actuators B*: *Chemical*, **156**, 918-923. https://doi.org/10.1016/j.snb.2011.03.006

[3] Herrera, M., Maestre, D., Cremades, A. and Piqueras, J. (2013) Growth and Characterization of Mn Doped SnO_2 Nanowires, Nanobelts, and Microplates. *The Journal of Physical Chemistry C*, **117**, 8997-9003. https://doi.org/10.1021/jp4007894

[4] Choi, S.W., Katoch, A., Sun, G.J., Wu, P. and Kim, S.S. (2013) NO_2-Sensing Performance of SnO_2 Microrods by Functionalization of Ag Nanoparticles. *Journal of Materials Chemistry C*, **1**, 2834-2841. https://doi.org/10.1039/c3tc00602f

[5] Tonezzera, M. and Hieu, N.V. (2012) Size-Dependent Response of Single-Nanowire

Gas Sensors. *Sensors and Actuators B*: *Chemical*, **163**, 146-152. https://doi.org/10.1016/j.snb.2012.01.022

[6] Shao, F., Hoffmann, M.W.G., Prades, J.D., Zamani, R., Arbiol, J. and Morante, J.R. (2013) Heterostructured p-CuO (Nanoparticle)/n-SnO_2 (Nanowire) Devices for Selective H_2S Detection. *Sensors and Actuators B*: *Chemical*, **181**, 130-135.

[7] Fang, X.S., Wu, L.M. and Hu, L.F. (2011) ZnS Nanostructure Arrays: A Developing Material Star. *Advanced Materials*, **23**, 585-598. https://doi.org/10.1002/adma.201003624

[8] Wang, L., Chen, Y., Ma, J., Chen, L., Xu, Z. and Wang, T. (2013) Hierarchical SnO_2 Nanospheres: Bio-Inspired Mineralization, Vulcanization, Oxidation Techniques, and the Application for NO Sensors. *Scientific Reports*, **3**, 3500.

[9] Wang, Y., Liu, B., Cai, D., Li, H., Liu, Y., Wang, D., Wang, L., Li, Q. and Wang, T. (2014) Room-Temperature Hydrogen Sensor Based on Grain-Boundary Controlled Pt Decorated In_2O_3 Nanocubes. *Sensors and Actuators B*: *Chemical,* **201**, 351-359 .

[10] Quang, V.V., Dung, N.V., Trong, N.S., Hoa, N.D., Duy, N.V. and Hieu, N.V. (2014) Outstanding Gas-Sensing Performance of Graphene/SnO_2 Nanowire Schottky Junctions. *Applied Physics Letters*, **105**, Article ID: 013107.

[11] Liu, X., Zhang, J., Guo, X., Wu, S. and Wang, S. (2010) Amino Acid-Assisted One-Pot Assembly of Au, Pt Nanoparticles Onto One-Dimensional ZnO Microrods. *Nanoscale*, **2**, 1178-1184. https://doi.org/10.1039/c0nr00015a

[12] Wang, H. and Rogach, A.L. (2014) Hierarchical SnO_2 Nanostructures: Recent Advances in Design, Synthesis, and Applications. *Chemistry of Materials*, **26**, 123-133. https://doi.org/10.1021/cm4018248

[13] Tricoli, A. and Pratsinis, S.E. (2010) Dispersed Nanoelectrode Devices. *Nature Nanotechnology*, **5**, 54-60. https://doi.org/10.1038/nnano.2009.349

[14] Cai, B., Zhao, X., Pei, T., Toninelli, E., Tang, Q., Tong, Y. and Liu, Y. (2014) Conductive SnO_2: Sb Nanobelts as Electrodes for Detection of NO_2 in Ppb Level with Ultrahigh Sensitivity. *Applied Physics Letters*, **104**, Article ID: 073112.

[15] Lu, G., Ocola, L.E. and Chen, J. (2009) Room-Temperature Gas Sensing Based on Electron Transfer between Discrete tin Oxide Nanocrystals and Multiwalled Carbon Nanotubes. *Advanced Materials*, **21**, 2487-2491. https://doi.org/10.1002/adma.200803536

[16] Li, X., Zhang, F. and Zhao, D. (2015) Lab on up Conversion Nanoparticles: Optical Properties and Applications Engineering via Designed Nanostructure. *Chemical Society Reviews*, **44**, 1346-1378. https://doi.org/10.1039/C4CS00163J

[17] Wang, H., Lu, W., Zeng, T., Yi, Z., Rao, L., Liu, H. and Zeng, S. (2014) Multi-Functional $NaErF_4$: Yb Nanorods: Enhanced Red Upconversion Emission, *in Vitro* Cell, *in Vivo* X-Ray, and T_2-Weighted Magnetic Resonance Imaging. *Nanoscale*, **6**, 2855-2860. https://doi.org/10.1039/c3nr05782h

[18] Epicier, T., Boulon, G., Zhao, W., Guzik, M., Jiang, B., Ikesuef, A. and Esposito, L. (2012) Spatial Distribution of the Yb^{3+} Rare Earth Ions in $Y_3Al_5O_{12}$ and Y_2O_3 Optical Ceramics as Analyzed by TEM. *Journal of Materials Chemistry*, **22**, 18221-18229. https://doi.org/10.1039/c2jm32995f

[19] Zhang, K.C., Li, Y.F., Liu, Y. and Chi, F. (2014) Density-Functional Study on the Robust Ferromagnetism in Rare-Earth Element Yb-Doped SnO_2. *Journal of Magnetism and Magnetic Materials*, **360**, 165-168. https://doi.org/10.1016/j.jmmm.2014.02.054

[20] Bouzidi, C., Elhouichet, H. and Moadhen, A. (2011) Yb^{3+} Effect on the Spectroscopic Properties of Er-Yb Codoped SnO_2 Thin Films. *Journal of Luminescence*, **131**,

2630-2635. https://doi.org/10.1016/j.jlumin.2011.06.040

[21] Wang, T.T., Ma, S.Y., Cheng, L., Luo, J., Jiang, X.H. and Jin, W.X. (2015) Preparation of Yb-Doped SnO_2 Hollow Nanofibers with an Enhanced Ethanol-Gas Sensing Performance by Electrospinning. *Sensors and Actuators B*: *Chemical*, **216**, 212-220.

[22] Chen, W.W., Liu, Y.K., Qin, Z.J., Wu, Y.M., Li, S.H. and Ai, P. (2015) A Single Eu-Doped In_2O_3 Nanobelt Device for Selective H_2S Detection. *Sensors*, **15**, 29950-29957. https://doi.org/10.3390/s151229775

[23] Qin, Z.J., Liu, Y.K., Chen, W.W., Ai, P., Wu, Y.M., Li, S.H. and Yu, D.P. (2016) Highly Sensitive Alcohol Sensor Based on a Single Er-Doped In_2O_3 Nanoribbon. *Chemical Physics Letters*, **646**, 12-17. https://doi.org/10.1016/j.cplett.2015.12.054

[24] Michel, C.R., Martínez-Preciadob, A.H. and Rivera-Tello, C.D. (2015) CO_2 Gas Sensing Response of YPO_4 Nanobelts Produced by a Colloidal Method. *Sensors and Actuators B*: *Chemical*, **221**, 499-506.

[25] Zhao, Z., Tian, J., Sang, Y., Cabot, A. and Liu, H. (2015) Structure, Synthesis, and Applications of TiO_2 Nanobelts. *Advanced Materials*, **27**, 2557-2582. https://doi.org/10.1002/adma.201405589

[26] Cheng, L., Ma, S.Y., Li, X.B., Luo, J., Li, W.Q., Li, F.M., Mao, Y.Z., Wang, T.T. and Li, Y.F. (2014) Highly Sensitive Acetone Sensors Based on Y-Doped SnO_2 Prismatic Hollow Nanofibers Synthesized by Electrospinning. *Sensors and Actuators B*: *Chemical*, **200**, 181-190.

[27] Samà, J., Barth, S., Domènech-Gil, G., Prades, J.D., Romano-Rodríguez, A., López N. and Casals, O. (2016) Site-Selectively Grown SnO_2 NWs Networks on Micromembranes for Efficient Ammonia Sensing in Humid Conditions. *Sensors and Actuators B*: *Chemical*, **232**, 402-409.

[28] Yang, W., Wan, P., Zhou, X.D., Hu, J.M., Guan, Y.F. and Feng, L. (2014) An Additive-Free Synthesis of In_2O_3 Cubes Embedded into Grapheme Sheets and Their Enhanced NO_2 Sensing Performance at Room Temperature. *ACS Applied Materials & Interfaces*, **6**, 21093-21100. https://doi.org/10.1021/am505949a

[29] Chen, P.C., Sukcharoenchoke, S., Ryu, K., Arco, L.G.D., Badmaev, A., Wang, C. and Zhou, C. (2010) 2, 4, 6-Trinitrotoluene (TNT) Chemical Sensing Based on Aligned Single-Walled Carbon Nanotubes and ZnO Nanowires. *Advanced Materials*, **22**, 1900-1904.

[30] Dua, V., Surwade, S.P., Ammu, S., Agnihotra, S.R., Jain, S., Roberts, K.E., Park, S. and Ruoff, R.S. (2010) Manohar, All-Organic Vapor Sensor Using Inkjet-Printed Reduced Graphene Oxide. *Angewandte Chemie*, **122**, 2200-2203. https://doi.org/10.1002/ange.200905089

[31] Yuan, W., Liu, A., Huang, L., Li, C. and Shi, G. (2013) High-Performance NO_2 Sensors Based on Chemically Modified Graphene. *Advanced Materials*, **25**, 766-771. https://doi.org/10.1002/adma.201203172

[32] Wagner, T., Haffer, S., Weinberger, C., Klaus, D. and Tiemann, M. (2013) Mesoporous Materials as Gas Sensors. *Chemical Society Reviews*, **42**, 4036-4053. https://doi.org/10.1039/C2CS35379B

[33] Xu, K., Zeng, D., Tian, S., Zhang, S. and Xie, C. (2014) Hierarchical Porous SnO_2 Micro-Rods Topologically Transferred from Tin Oxalate for Fast Response Sensors to Trace Formaldehyde. *Sensors and Actuators B*: *Chemical*, **190**, 585-592.

[34] Li, Y.S., Xu, J., Chao, J.F., Chen, D., Ouyang, S.X., Ye, J.H. and Shen, G.Z. (2011) High-Aspect-Ratio Single-Crystalline Porous In_2O_3 Nanobelts with Enhanced Gas Sensing Properties. *Journal of Materials Chemistry*, **21**, 12852-12857. https://doi.org/10.1039/c1jm11356a